

Chapter 3

SI MICROWIRE-ARRAY PHOTOCATHODES DECORATED WITH CU ALLOW CO₂ REDUCTION WITH MINIMAL PARASITIC ABSORPTION OF SUNLIGHT

Kempler, P. A., Richter, M. H., Cheng, W.H., Brunschwig, B.S., & Lewis, N.S. (2020).

Si Microwire-Array Photocathodes Decorated with Cu Allow CO₂ Reduction with Minimal Parasitic Absorption of Sunlight. *ACS Energy Letters*, 5(8), 2528-2534.

<https://doi.org/10.1021/acsenergylett.0c01334>

3.1 Introduction

Electrochemical reduction of carbon dioxide, CO₂R, to carbon monoxide,⁷⁰⁻⁷¹ methane, ethylene,⁷²⁻⁷³ and other reduced hydrocarbons and oxygenates provides a method of converting an industrial waste product into a feedstock for commodity chemicals and fuels.⁷⁴ Both the activity and selectivity towards the generation of hydrocarbons can be controlled via the preparation of new intermetallic and alloy materials,⁷⁵ but the sum of the absolute partial current densities towards hydrocarbons, $|j_{\text{HC}}|$, at such catalysts is typically $< 1 \text{ mA}\cdot\text{cm}^{-2}$ at overpotentials $< 0.5 \text{ V}$.⁷⁶⁻⁷⁷ Under 1 atm of CO₂(g) and modest overpotentials, $< 0.5 \text{ V}$, the reduction of CO₂ is kinetically limited as opposed to mass-transport limited. Therefore, at a given potential, use of nanostructured, high surface area catalysts will yield an increased $|j_{\text{HC}}|$.⁷⁸⁻⁷⁹

Photoelectrochemical CO₂R, wherein accumulated photogenerated charge carriers lead to a positive shift in the potential required to effect the electrochemical reduction, requires appropriate integration of semiconductors and catalysts.¹⁹ Nanostructured semiconductors have previously been used as photocathodes for CO₂R that produce CO, but not hydrocarbons. Silicon decorated with Ag nanoparticles during metal-assisted chemical etching was illuminated with 50 mW·cm⁻² of simulated sunlight and exhibited absolute photocurrent densities of 8 mA·cm⁻² at -0.5 V vs. the reversible hydrogen electrode (RHE), with > 80% Faradaic efficiency towards CO.⁸⁰ Silicon nanowires decorated with Au₃Cu nanoparticles and under 20 mW·cm⁻² of 740 nm illumination exhibited an absolute photocurrent density > 5.5 mA·cm⁻² at -0.4 V vs. RHE with 67% Faradaic efficiency towards CO.⁸¹ The generation of hydrocarbons has been reported at Si-based photocathodes, but when the catalyst is loaded on the light-facing side of the photoelectrode absolute photocurrent densities, $|J_{ph}|$, have been limited to < 2 mA·cm⁻² at potentials less negative than -1.0 V vs. RHE.⁸²⁻⁸³ Larger absolute photocurrent densities can be obtained when the catalyst is not in the path of incident illumination. For example, a Cu-Ag alloy has been integrated onto the dark-facing side of a p⁺nn⁺-Si light absorber and produced $|J_{ph}| > 30$ mA·cm⁻² at -1.1 V vs. RHE under 100 mW·cm⁻² of Air Mass (AM) 1.5 simulated sunlight.⁸⁴

Herein, we investigate whether Si μ W-arrays can minimize trade-offs between catalyst loading and light collection for light-facing photocathodes effecting CO₂R to hydrocarbons. We demonstrate a Si photocathode with Cu electrodeposited onto the vertical sidewalls of high-aspect ratio microwires that exhibits minimal parasitic absorption by the catalyst with a maximum $|J_{ph}| > 25$ mA·cm⁻² before and after 48 h of

photoelectrochemical CO₂R conditions, leading to the generation of C₂H₄ at more positive potentials than previously reported for photocathodes under 1-Sun illumination. The positive shift in the onset potential for C₂H₄ production, relative to that of a polished Cu foil electrode, exceeded the photovoltage of the n⁺p-Si μW array electrode due to the increased surface area within the internal volume of the μW array. An analytical expression is presented to express the effect of microstructure on the current density vs. potential (*J-E*) behavior of a photoelectrode, as a function of the diode quality factor of the semiconductor and the Tafel slope of the electrocatalyst.

3.2 Experimental Methods

(Photo)electrodepositions of Catalyst: Prior to electrodeposition of Cu, electrodes were rinsed sequentially with acetone, isopropyl alcohol, methanol, and deionized water and then dipped into buffered oxide etchant for 60 s. Electrodepositions were controlled with a BioLogic SP-200 potentiostat. The Cu-plating bath was continuously purged with Ar(g) and contained 0.10 M CuSO₄(aq), 5.0 mM H₂SO₄(aq), and 0.10 M K₂SO₄(aq), at a pH of ~3. A saturated calomel electrode (SCE, CH Instruments) was used as a reference and the counter electrode was a high-purity graphite rod (Alfa Aesar, 5N) (**Figure 3.1A**). The illumination source was an array of narrowband light-emitting diodes (Luxeon Rebel Blue SMD, FWHM 22 nm) with a peak intensity at 465 nm. The illumination wavelength was selected to maximize transmission of light through the colored electrolyte. Cu was deposited potentiostatically at 0.0 V vs. SCE until the desired charge density had passed, normalized to the projected area of the electrode.

Photoelectrochemical CO₂ Reduction Testing: The electrochemical setup was operated in a continuous flow mode. Carbon dioxide was provided to the electrochemical cell at a

flow rate of 5 sccm as controlled by an Alicat flow controller. The carbon dioxide stream was supplied as humidified CO₂ with a gas bubbler placed between the cell and flow controller. The exhaust gases went through a liquid trap, then an Alicat flow meter, and finally to a gas chromatograph (SRI-8610) using a Hayesep D column and a Molsieve 5A column with N₂ as the carrier gas. The gaseous products were detected using a thermal conductivity detector (TCD) and a flame ionization detector (FID) equipped with a methanizer. Quantitative analysis of gaseous products was based on calibrations with several gas standards over many orders of magnitude in concentration. The calibrations were used to calculate the partial current density, j , towards products of the CO₂R and hydrogen evolution reaction. To measure liquid products, the electrolyte on the anode and cathode sides of the cell was sampled at the end of the run and was analyzed by high-performance liquid chromatography (HPLC, Thermo Scientific Ultimate 3000). Products were not quantified in Faradaic efficiency calculations because continuous purging of the catholyte with CO₂ expelled accumulated products. Moreover, crossover of products to the anolyte was observed and oxidation at the anode could potentially occur. An Oriel Instruments 75 W Solar Simulator supplied 100 mW·cm⁻² of AM 1.5 illumination. The light intensity was calibrated using the measured photocurrent at a calibrated (350 to 1100 nm, 1 cm²) NIST traceable Si photodiode (Thorlabs FDS1010-CAL) mounted within the testing cell prior to the addition of the electrolyte.

3.3 Results

Figure 3.1 compares the photoelectrochemical behavior of planar n⁺p-Si to the behavior of a radially doped n⁺p-Si μW-array electrode. A schematic of the photoelectrochemical cell is presented in **Figure 3.1A**. A comparison of the J - E behavior

of illuminated planar n^+p -Si/Cu and n^+p -Si μ W/Cu electrodes in the plating cell before and after, respectively, $-1.00 \text{ C}\cdot\text{cm}^{-2}$ of charge passed towards Cu deposition is presented in **Figure 3.1B**. For the planar n^+p -Si electrode, $|J_{\text{ph}}|$ at -0.2 V vs. the saturated calomel electrode (SCE) decreased by 29% of its initial value, whereas $|J_{\text{ph}}|$ for the μ W-array electrode remained unchanged from its initial value. The photocurrent at 0.0 V vs. SCE versus Cu loading, as measured by the cathodic charge density passed, is presented in **Figure 3.1C**. Initially, both the planar and μ W electrode had similar photocurrent densities. However, for the planar, n^+p -Si, $|J_{\text{ph}}|$ continuously decreased with increased loadings of Cu, whereas at the n^+p -Si μ W electrode, $|J_{\text{ph}}|$ increased and then remained nearly constant. Planar and μ W electrodes exhibited $|J_{\text{ph}}| = 17.9$ and $26.0 \text{ mA}\cdot\text{cm}^{-2}$ after -148 and $-1000 \text{ C}\cdot\text{cm}^{-2}$, respectively, had been passed towards Cu deposition. These geometric charge densities were equivalent after renormalization to the greater microstructured area of the μ W array and thus the photoelectrochemical behavior was not solely a function of microstructured area.

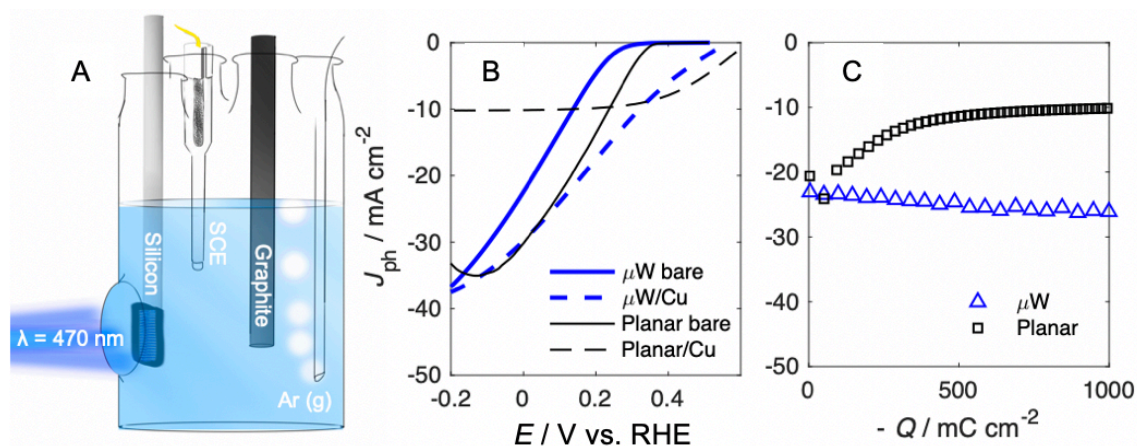


Figure 3.1: (A) Cell schematic for the photoelectrochemical deposition of Cu onto n^+p -Si. (B) Photoelectrochemical $J_{\text{ph}}-E$ behavior of n^+p -Si μW (blue lines) and planar n^+p -Si (black lines) in an Ar purged Cu deposition bath, before (solid) and after (dashed) passage of $-1.00 \text{ C}\cdot\text{cm}^{-2}$. Linear sweep voltammograms were recorded at $-200 \text{ mV}\cdot\text{s}^{-1}$. (C) $J_{\text{ph}}-Q$ behavior for n^+p -Si μW and planar n^+p -Si during photoelectrochemical deposition of Cu at 0.0 V vs. SCE.

Scanning-electron micrograph, SEM, images of electrodeposited Cu on planar n^+p -Si and n^+p -Si μW electrodes are presented as **Figure 3.2**. On the planar electrode, Cu electrodeposited as discontinuous particles that began to merge at high loadings, leading to nearly continuous islands that were distributed unevenly and were prone to delamination (**Figure 3.2A-B**). In contrast, on n^+p -Si μW electrodes, nominally identical Cu loadings, as measured by the geometric charge density passed, led to discontinuous catalyst films that were distributed across the tips, sidewalls, and base of the μW array (**Figure 3.2C**). The Si μW -array was composed of cylinders with a nominal diameter, pitch, and height of 3, 7, and 30 μm , respectively, leading to a microstructured area 6.8 times that of a planar surface. A few Cu particles $\sim 5 \mu\text{m}$ in diameter were visible on the tips of individual wires (**Figure 3.2D**).

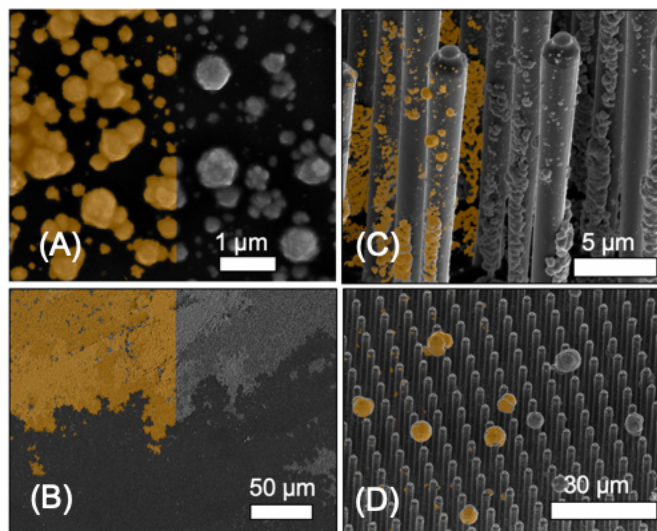


Figure 3.2: False-color SEM images of Cu (orange) photoelectrodeposited onto planar n^+p Si after (A) $-148 \text{ mC}\cdot\text{cm}^{-2}$ (B) and $-1.00 \text{ C}\cdot\text{cm}^{-2}$ geometric charge density had been passed. (C-D) n^+p -Si μW after a geometric charge density of $-1.00 \text{ C}\cdot\text{cm}^{-2}$ had been passed.

The n^+p -Si μW /Cu electrodes were evaluated as photocathodes for CO_2R , with online GC-FID/TCD detection of gaseous products, to determine the activity of the microstructured catalyst film and the effects of the photovoltage on the product distribution. **Figure 3.3A** compares the J - E behavior of an electropolished Cu foil in the dark to an illuminated n^+p -Si μW /Cu electrode in 0.10 M KHCO_3 saturated with $\text{CO}_2(\text{g})$ at 1 atm . Illumination produced a substantial positive shift in the onset of cathodic current, with a saturated $|J_{\text{ph}}|$ of $31 \pm 3 \text{ mA}\cdot\text{cm}^{-2}$ observed at -0.62 V vs. RHE. The partial current density behaviors, j_x - E , of Cu deposited on n^+p -Si μW catalyzing the formation of CO , CH_4 , and C_2H_4 consistently shifted towards more positive potentials, with the magnitude of the shift varying for different reduction products (**Figures 3.3-3.4**). The activity of n^+p -Si μW /Cu electrodes towards H_2 was larger than that of a Cu foil (**Figure 3.4**).

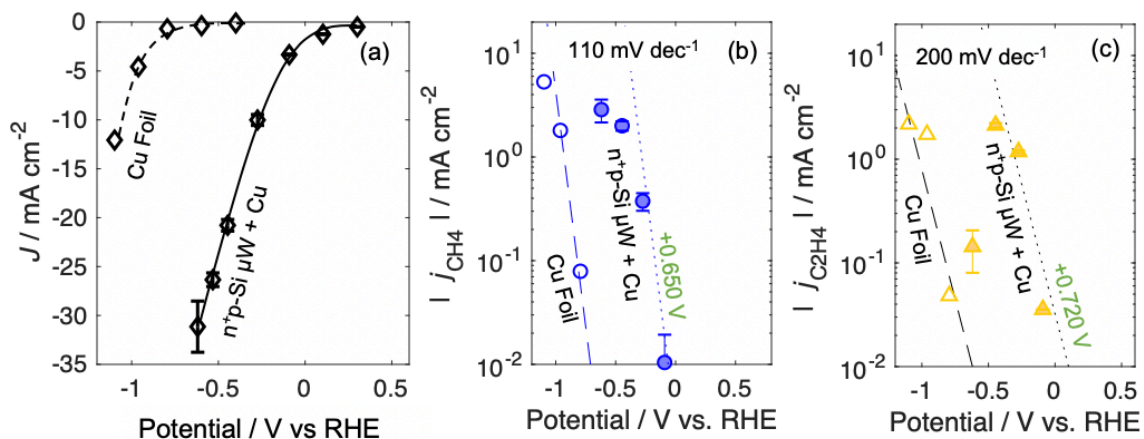


Figure 3.3: (A) J - E behavior of electropolished Cu (open markers) in 0.10 M KHCO₃(aq) to the photoelectrochemical J_{ph} - E behavior of n⁺p-Si μW (filled markers) under 100 mW·cm⁻² simulated sunlight in a nominally identical electrochemical cell. (B) Absolute partial current density towards CH₄ vs. potential, j_{CH_4} - E , behavior measured via online GC-FID/TCD, for electropolished Cu and n⁺p-Si μW. (C) Absolute partial current density towards C₂H₄ vs. potential, $j_{\text{C}_2\text{H}_4}$ - E , behavior measured via online GC-FID/TCD, for electropolished Cu and n⁺p-Si μW. Guidelines in (B,C) represent predicted behavior from measured Tafel slopes and photovoltages (*vide infra*).

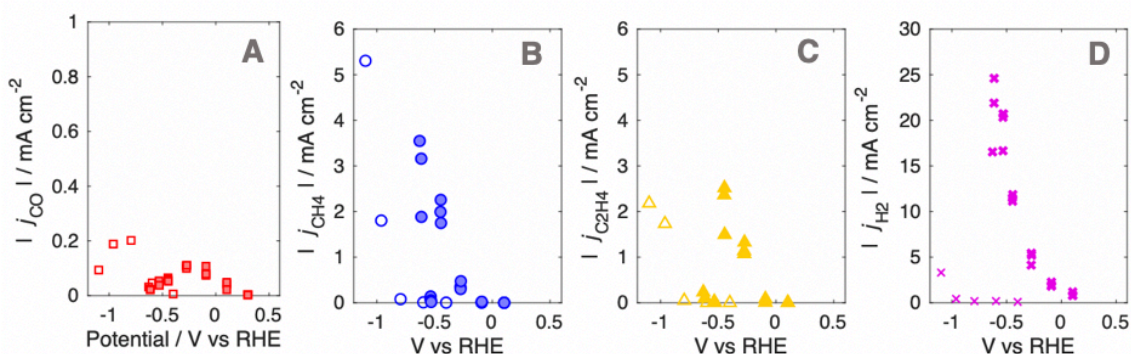


Figure 3.4: Plots of the partial current densities towards (photo)electrochemical CO₂R products vs. potential for n⁺p-Si μW/Cu electrodes (filled markers) compared to planar Cu electrodes (open markers). (A) j_{CO} - E behavior for production of CO, (B) j_{CH_4} - E behavior for production of CH₄, (C) $j_{\text{C}_2\text{H}_4}$ - E behavior for production of C₂H₄, and (D) j_{H_2} - E behavior for production of H₂, detected by online GC-FID/TCD.

The n⁺p-Si μW/Cu electrode exhibited a peak $|j_{\text{C}_2\text{H}_4}|$ of $2.1 \pm 0.2 \text{ mA}\cdot\text{cm}^{-2}$ at a potential of -0.44 V vs. RHE, and the peak $|j_{\text{CH}_4}|$ of $2.9 \pm 0.7 \text{ mA}\cdot\text{cm}^{-2}$ was observed at -0.62 V vs. RHE. The total $|j_{\text{HC}}|$ at $E = -0.44 \text{ V}$ vs. RHE was $4.1 \pm 0.2 \text{ mA}\cdot\text{cm}^{-2}$. Onset potentials for H₂ and CO were positive of RHE, while those for C₂H₄ and CH₄ generation were observed at -0.09 V vs. RHE.

Delamination of Cu films from planar n⁺p-Si/Cu electrodes during electrolysis led to increasing photocurrents and decreasing activity towards photoelectrochemical CO₂R. The average j_{CH_4} was $-0.9 \pm 0.3 \text{ mA}\cdot\text{cm}^{-2}$ and $-0.7 \pm 0.3 \text{ mA}\cdot\text{cm}^{-2}$, during the first 10 min of electrolysis, for n⁺p-Si/Cu photoelectrodes having a catalyst loading of $-148 \text{ mC}\cdot\text{cm}^{-2}$ and $-1.00 \text{ C}\cdot\text{cm}^{-2}$, respectively. The declined activity of planar n⁺p-Si/Cu electrodes within the first 20 min of controlled potential electrolysis prevented a quantitative assessment of the J - E behavior. The loss in activity was likely due to passivation of the Si/Cu interface and/or more rapid poisoning of the reduced catalyst surface area relative to the behavior of Cu in Si μW-arrays.

The stability of n⁺p-Si μW/Cu electrodes was investigated via extended chronoamperometry at -0.58 V vs. RHE under $100 \text{ mW}\cdot\text{cm}^{-2}$ of Air Mass (AM) 1.5 simulated sunlight (details on intensity calibrations are provided in the Appendix, **A.3**). After an initial increase in $|J_{\text{ph}}|$ upon reduction of Cu to its metallic state, the maximum photocurrent density remained stable for 48 h under constant potential (**Figure 3.5A**). The J - E behavior of the n⁺p-Si μW/Cu electrode, as measured via linear sweep voltammetry at a scan rate of $-50 \text{ mV}\cdot\text{s}^{-1}$ at 4 h intervals during the chronoamperometry, indicated that the optical properties of the integrated Si/Cu microstructure, the photovoltage of the n⁺p-Si junction, and the electrical resistance of the Si/Cu interface remained stable after a brief

initial period of activation (**Figure 3.5A**). Greater than 90% of the photocurrent density eventually resulted in the formation of $\text{H}_2(\text{g})$ (**Figure 3.5C**). During continuous potential control of $\text{n}^+\text{p-Si } \mu\text{W/Cu}$ electrodes at -0.58 V vs. RHE , $|j_{\text{C}_2\text{H}_4}|$ and $|j_{\text{CH}_4}|$ decreased after 4 and 8 h, respectively, whereas $|j_{\text{CO}}|$ increased with time (**Figure 3.5D**).

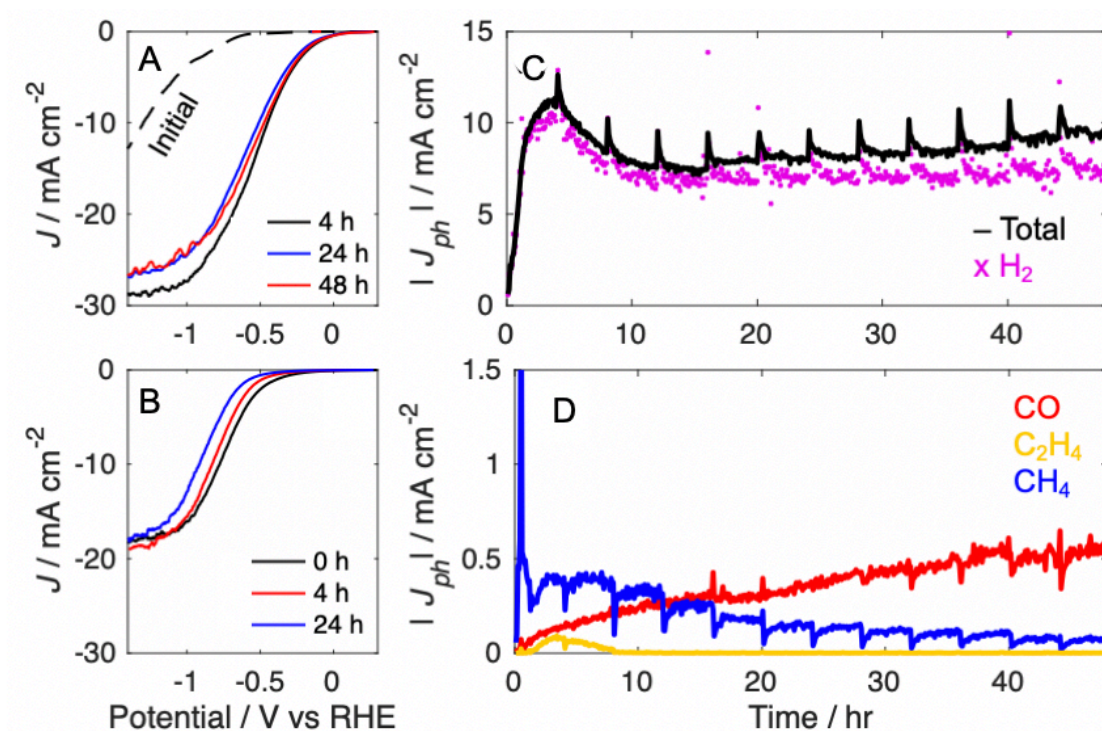


Figure 3.5: Photoelectrochemical data for $\text{n}^+\text{p-Si Cu}$ electrodes during stability evaluation at -0.58 V vs. RHE in CO_2 -purged $0.10 \text{ M KHCO}_3(\text{aq})$ under $100 \text{ mW}\cdot\text{cm}^{-2}$ simulated sunlight. **(A-B)** Time dependent J - E behavior for a **(A)** $\text{n}^+\text{p-Si } \mu\text{W/Cu}$ electrode and **(B)** planar $\text{n}^+\text{p-Si/Cu}$ electrode, loaded with -1.00 and -0.148 C cm^{-2} , respectively, as measured by a linear sweep voltammogram recorded at a scan rate of $50 \text{ mV}\cdot\text{s}^{-1}$. **(C)** Absolute photocurrent density and partial photocurrent density towards $\text{H}_2(\text{g})$, as measured via GC-FID/TCD, represented as black x's and a gray line, respectively for a $\text{n}^+\text{p-Si } \mu\text{W/Cu}$ electrode. **(D)** Absolute partial photocurrent density towards $\text{CO}(\text{g})$, $\text{C}_2\text{H}_4(\text{g})$, and $\text{CH}_4(\text{g})$ presented as red, gold, and blue lines, respectively for a $\text{n}^+\text{p-Si } \mu\text{W/Cu}$ electrode.

Aqueous products were collected from the electrolyte in the cathode and anode compartments at the conclusion of the 48 h chronoamperometry stability experiment and were analyzed via HPLC. SEM images of the n^+p -Si μ W electrode (**Figure 3.6**) showed that the morphology of the deposited Cu catalyst particles changed during extended chronoamperometry, whereas the morphology of the Si μ W-array electrode remained unchanged.

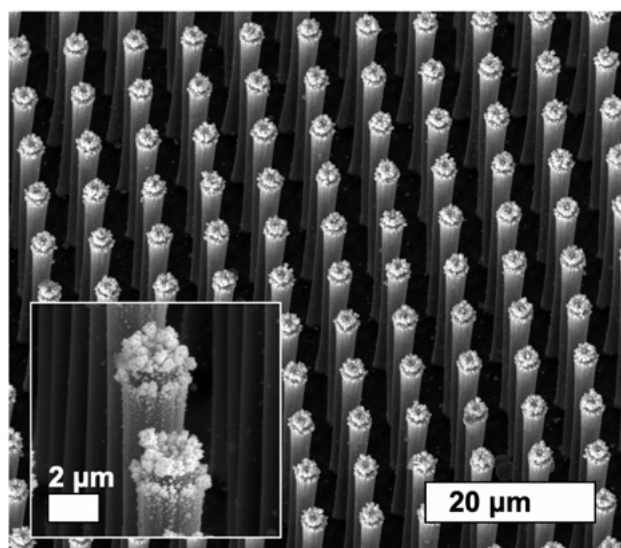


Figure 3.6 SEM of an n^+p -Si- μ W/Cu photocathode after 96 h of continuous photoelectrochemical operation in CO_2 -purged 0.10 M $\text{KHCO}_3(\text{aq})$ under $100 \text{ mW}\cdot\text{cm}^{-2}$ of simulated sunlight. Primary scale bar represents 20 μm , inset scale bar represents 2 μm .

3.4 Discussion

Arrays of vertically-oriented Si μ Ws allow for high mass loadings of electrodeposited Cu on the light-facing side of photoelectrodes without substantial reductions in $|J_{\text{ph}}|$ (**Figure 3.1C**). Despite the high ($0.33 \text{ mg}\cdot\text{cm}^{-2}$) mass loading of electrocatalyst on the light-facing side of the electrode (Equation A.3.1), n^+p -Si μ W/Cu

electrodes exhibited absolute photocurrent densities $> 30 \text{ mA}\cdot\text{cm}^{-2}$ under AM 1.5 simulated solar illumination. The predicted $|J_{\text{ph}}|$ at a $500 \mu\text{m}$ thick Si slab in air, under AM 1.5 simulated solar illumination is $29 \text{ mA}\cdot\text{cm}^{-2}$ and uncovered, planar $\text{n}^+\text{p-Si}$ in $0.50 \text{ M H}_2\text{SO}_4(\text{aq})$ under AM 1.5 simulated solar illumination exhibited a limiting $|J_{\text{ph}}|$ of 27.5 mA cm^{-2} .^{44, 63} The generation rate of hydrocarbons at $\text{n}^+\text{p-Si } \mu\text{W/Cu}$ electrodes in $0.10 \text{ M KHCO}_3(\text{aq})$ saturated with $\text{CO}_2(\text{g})$ matched or exceeded the performance of an electrode possessing the electrocatalytic activity of an electropolished Cu film in series with the photovoltage of a microstructured Si photovoltaic (**Figure 3.3-3.4**).

The yield of hydrocarbon and oxygenate products in the (photo)electrochemical CO_2R is a function of both the catalyst used and the overpotential. Decreasing the coverage of catalysts on a photoelectrode can lead to increased light transmission, photocurrent, and photovoltage but will adversely affect the total rate of reaction if kinetic losses at the catalysts are not overcome by the increased photovoltage. Furthermore, the regions responsible for catalysis and light absorption must be within the diffusion length of the excited charge carriers to prevent losses due to carrier recombination. Microstructured semiconductors provide additional surface area for light collection and electrocatalysis, but must overcome a reduction in photovoltage due to the increased surface area available for recombination. The photovoltage, V_{ph} , provided by a microstructured semiconductor with a junction uniformly distributed across the surface is described by **Equation 3.1**:

$$V_{\text{ph}}(J) = \frac{2.3nk_bT}{q} \log_{10} \left(\frac{|J_{\text{ph}}| - |J|}{(R_{\mu})|J_0|} + 1 \right) \quad (3.1)$$

where n is the diode quality factor, k_b is Boltzmann's constant, T is the operating temperature, q is the unsigned elementary charge, J_0 is the dark current density across the charge-separating junction, and R_{μ} is the ratio of the microstructured area to the geometric

area. Current densities are normalized to the geometric area of the device. **Equation 3.2** represents the η - J relationship at electrocatalysts on a microstructured electrode as described by the Tafel equation:

$$\eta(J) = b \log_{10}(|J|/R_{\mu}) - a \quad (3.2)$$

where b is the measured Tafel slope and a can be calculated from the measured exchange current density.⁴⁷

The effect of increasing the microstructured area of a photoelectrode on the illuminated j - E behavior can be described by the sum of **Equations 3.1** and **3.2**. Increasing the microstructured area at an ideal diode ($n = 1$) leads to a $60 \text{ mV}\cdot\text{dec}^{-1}$ reduction in $|V_{\text{ph}}|$, whereas the reduction in $|\eta|$ depends on the Tafel slope of the catalyst (**Figure 3.6A**). The Tafel slopes for Cu catalyzing CO_2R to CH_4 and C_2H_4 in $0.50 \text{ M KHCO}_3(\text{aq})$ have been reported as $110 \text{ mV}\cdot\text{dec}^{-1}$ and $200 \text{ mV}\cdot\text{dec}^{-1}$, respectively.²⁶ Hence microstructured photocathodes prepared from ideal diodes decorated with Cu will produce C_2H_4 at more positive potentials than an equivalent planar photocathode (**Figure 3.6B**). For catalysts that exhibit small Tafel slopes $< 60 \text{ mV}\cdot\text{dec}^{-1}$, e.g. Pt effecting the HER at pH 0 ($b = 28 \text{ mV}\cdot\text{dec}^{-1}$), reductions in photovoltage will match or exceed reductions in the overpotential that result from microstructuring, leading to a negative potential shift in the j - E behavior (**Figure 3.6B**). For $b = 60 - 120 \text{ mV}\cdot\text{dec}^{-1}$ the net effect of microstructuring depends on n , while for $b > 120 \text{ mV}\cdot\text{dec}^{-1}$, in the absence of mass transport limitations, reductions in V_{ph} will typically be fully offset by reductions in η (**Figure 3.6C**).

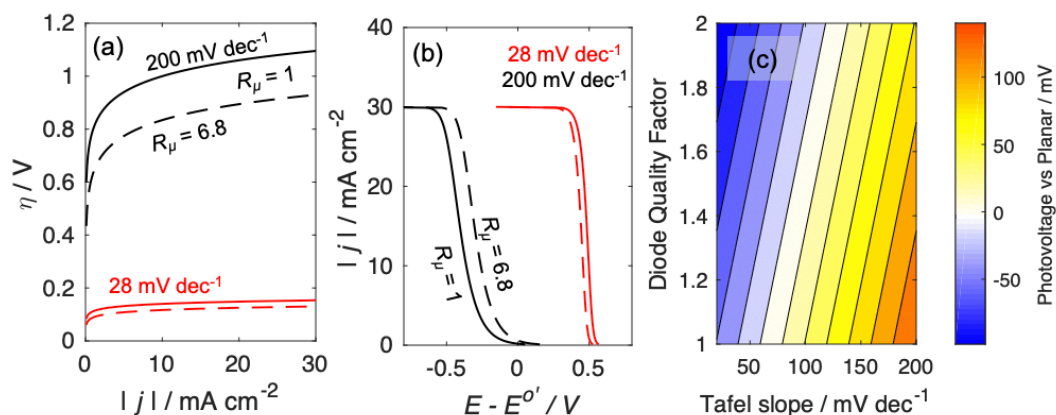


Figure 3.6: (A) η - J behavior for planar ($R_\mu = 1$), continuous lines, and μ W ($R_\mu = 6.8$), dashed lines, for electrocatalysts exhibiting $b = 0.028$ and $0.200\ V\cdot dec^{-1}$, shown in red and black, respectively. (B) j - E behavior calculated from the sum of Equations 1 and 2 for planar, continuous lines, and μ W, dashed lines, photocathodes as a function of b , for $J_{ph} = 30\ mA\cdot cm^{-2}$ and $n = 1.3$. (C) Contour lines comparing the shift in photovoltage at $|J_{ph}| = 10\ mA\cdot cm^{-2}$, due to increasing R_μ by a factor of 10, as a function of n and b . Details on the calculations are provided in the Appendix, A.3.

The observations herein demonstrate that microstructured photoelectrodes can yield a positive shift in the j - E behavior in excess of the photovoltage of a planar semiconductor, thereby increasing j_{CO_2R} . Semi-log plots of $|j_{CH_4}|$ and $|j_{C_2H_4}|$ versus E for planar and μ W n^+p -Si electrodes exhibited mutually similar Tafel slopes that were moreover in agreement with literature values (**Figure 3.3B-C**).⁸⁵ Over a range of photocurrent densities relevant to solar-fuels device operation, planar n^+p -Si junctions ($R_\mu = 1$) exhibited $n = 1.3$ and $J_0 = 9 \times 10^{-10}\ A\cdot cm^{-2}$, whereas μ W n^+p -Si junctions ($R_\mu = 6.8$) exhibited $n = 2.5$ and $J_0 = 7 \times 10^{-7}\ A\cdot cm^{-2}$ (**Figure A.3**). The value of J_0 increased for the radial-junction relative to the planar junction, possibly as a consequence of the reactive-etching process. This explanation is consistent with the large value of n observed at the

μW junction. Relative to the planar $\text{n}^+\text{p-Si}$ junction, the reduction in $|V_{\text{ph}}|$ obtained at the μW $\text{n}^+\text{p-Si}$ junction was less than the expected V_{ph} based on changes to J_o , due to the simultaneous increase in n . At $|J_{\text{ph}}|$ comparable to those observed under simulated sunlight ($30 \text{ mA}\cdot\text{cm}^{-2}$), the μW junction yielded a V_{ph} that was 14 mV less than the planar junction. Based on the increased catalyst area and the measured V_{ph} , the predicted potential shifts in j_{CH_4} and $j_{\text{C}_2\text{H}_4}$ at the μW $\text{n}^+\text{p-Si/Cu}$ electrode are 0.650 and 0.720 V, respectively. The $j_{\text{C}_2\text{H}_4}$ - E data were in close agreement with the predicted values, while the j_{CH_4} - E data were shifted less positive, relative to polycrystalline Cu, than the predicted shift (**Figure 3.3B-C**). Details on the calculations of the potential shift in j_x - E are provided in the Appendix, **A.3**.

The onset of photocurrent at front-side illuminated $\text{n}^+\text{p-Si}$ $\mu\text{W/Cu}$ electrodes was observed at potentials $> 1 \text{ V}$ more positive than those previously reported at p-Si/Cu electrodes.⁸³ Planar $\text{n}^+\text{p-Si}$ with Cu at low or high catalyst loadings did not produce C_2H_4 in quantities sufficient for quantification and exhibited $j_{\text{CH}_4} < 0.5 \text{ mA}\cdot\text{cm}^{-2}$ within 20 min of potential control at -0.598 V vs. RHE. This behavior indicates that Cu loadings suitable for transmission of light on planar surfaces have low activity and/or electrochemical stability towards CO_2R . Glass with a 45 nm Cu film reflects $> 90\%$ of photons at wavelengths $> 600 \text{ nm}$ and $> 50\%$ of photons at wavelengths between 400–600 nm.⁸⁶ $|J_{\text{ph}}|$ values obtained at planar and μW $\text{n}^+\text{p-Si/Cu}$ photocathodes were larger than what would be expected given coverage of the surface with a continuous film, consistent with the discontinuous coating of opaque metal islands observed via SEM (**Figure 3.2B**). Semiconductors that cannot be readily microstructured or which exhibit high diode quality factors could benefit from the use of transparent, high surface-area, conductive supports for metallic catalysts for CO_2R .⁸⁷

High photocurrent densities were sustained at n⁺p-Si μW/Cu photocathodes for 48 h of photoelectrochemical operation, demonstrating that the exposed Si surfaces were passivated towards dissolution and that the electrical contact between the light-absorber and catalyst islands was stable (**Figures 3.4**). Prior experimental results on the electrocatalytic activity of Cu towards CH₄ and C₂H₄ in 0.1 M KHCO₃(aq) have been assessed on timescales ≤ 1 h, commensurate with the stability of photoelectrodes in this work.^{73, 88} Experiments conducted in flowing electrolytes have yielded Faradaic efficiencies which are significantly more stable towards CO₂R. A $|j_{\text{CO}}| > 130 \text{ mA cm}^{-2}$ was demonstrated for 100 h at PTFE-supported Ag in flowing 1 M KOH(aq).⁸⁹ Carbon-nanoparticle-supported Cu has yielded $|j_{\text{C}_2\text{H}_4}| \geq 50 \text{ mA cm}^{-2}$ for 150 h in flowing 7 M KOH(aq).⁹⁰ Increases in j_{H_2} and j_{CO} with time at n⁺p-Si μW/Cu photocathodes could be due to deposition of metal impurities from the solution either onto the Cu surface, reducing the catalytic efficiency of the Cu for CO₂R, or deposition onto the bare Si surface increasing its catalytic efficiency for H₂ and CO (**Figure 3.4**). Crossover of dissolved Pt from the anode to the Cu or Si surface could play this role. Inductively-coupled plasma mass-spectrometry and XPS, following a 5 day galvanostatic experiment at 10 mA in 0.10 M KCHO₃(aq) using a Pt foil anode and graphite cathode separated by a Selemion AMV membrane confirmed the presence of dissolved Pt in the anolyte and catholyte, and plating of metal onto the graphite surface (**Figure 3.7**). The graphite cathode was chosen so that peaks in the Pt 4f region of the XPS data could be resolved without interference from the substantially more intense Cu 3p peak. Photoelectrochemical cells that use the same catalyst for both CO₂R and water oxidation have been beneficially used to avoid such poisoning.⁹¹

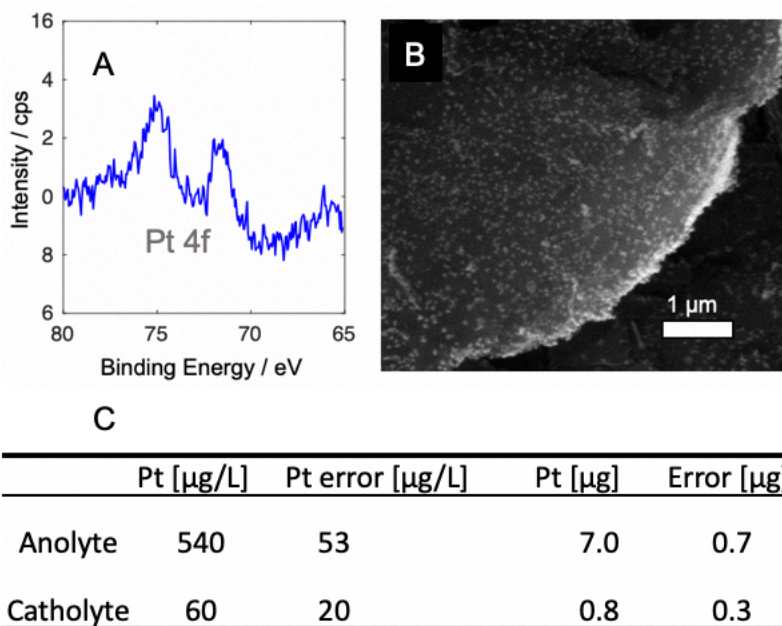


Figure 3.7: (A) X-ray photoelectron spectra of the surface of a graphite cathode in the Pt 4f region after 5 days under galvanostatic control at -10 mA in 0.10 M $\text{KHCO}_3(\text{aq})$. The graphite cathode was separated from a Pt anode by a Selemion membrane. (B) SEM image of the surface of the graphite surface measured in (A). Small metal nanoparticles, visible as white dots, were not present prior to the galvanostatic experiment. (C) Dissolved Pt concentration in the anolyte and catholyte, measured via inductively-coupled plasma mass-spectrometry, following a 5 day experiment with a constant current of 10 mA applied between a Pt foil anode and graphite cathode separated by Selemion AMV membrane.

Backside illuminated, textured Si photocathodes exhibit a $|j_{\text{HC}}|$, of $< 2 \text{ mA}\cdot\text{cm}^{-2}$ at -0.4 V vs. RHE.²⁵ Although the $\text{n}^+\text{p-Si } \mu\text{W/Cu}$ photocathodes reported herein exhibited a larger total $|j_{\text{HC}}| > 4 \text{ mA}\cdot\text{cm}^{-2}$ at -0.44 V vs. RHE, substantially lower Faradaic efficiencies were observed towards CO_2R relative to these previous reports. Cu supported on Ag has been shown to suppress the generation of $\text{H}_2(\text{g})$ such that greater Faradaic efficiencies towards hydrocarbons can be obtained.³³ CuAg alloys could be integrated onto Si μW -arrays to reduce the partial current density towards H_2 ,⁹² but at backside illuminated Si

photocathodes the HER was not suppressed without complete coverage of the photocathode surface by catalyst,⁸⁴ which is incompatible with the microstructuring strategy employed herein. Alternatively, suppression of the parasitic photocurrent density towards H₂ by passivation of the exposed light absorbing regions with an insulating, chemically inert layer such as SiN_x could lead to increased photovoltages and Faradaic efficiencies for CO₂R.⁹³

The results from this work have important applications in designs for electrode systems that use H₂O and CO₂ to store sunlight as fuels. Mass loadings of Cu, sufficient to meet the *j-E* behavior of a Cu foil, can be deposited on the light-absorbing surface of a microstructured photocathode for which the reduction in overpotential due to the microstructured surface area can meet or exceed the reductions in photovoltage due to increased dark current. Microstructured semiconductors will be required to ensure efficient and stable solar fuels generation so that membranes can be incorporated at length scales smaller than the minority-carrier diffusion length in the semiconductor.²² Although the Si μ W arrays in this work were formed via reactive-ion etching, similar structures can be grown from gas precursors such as SiCl₄ and SiH₄, over large areas, and have been used as efficient photocathodes.²⁹

Electrochemical reactions that consume protons generate pH gradients that can lead to shifts in the product distribution. Previous studies on micro- and nanostructured cathodes have used proton-concentration gradients to suppress the hydrogen-evolution reaction and increase the Faradaic efficiency of Au towards CO production.⁹⁴⁻⁹⁵ The short, sparse microwire array used in this work exhibited a similar product distribution relative to the polished Cu foil. The Tafel slopes were also mutually similar for both types of electrodes.

Future studies on densely packed microwire arrays with heights greater than the boundary layer thickness would enable the effects of concentration gradients of protons and $\text{CO}_2(\text{aq})$ within the electrode to be explored. In this work, photocathodes were operated under 1 atm of CO_2 and at near-neutral pH. In contrast, practical devices will require a concentrated source of CO_2 , higher pH values, forced convection of the electrolyte to minimize the thickness of the concentration boundary layer, and/or methods of interconverting HCO_3^- (aq) and $\text{CO}_2(\text{aq})$ to sustain $|J_{\text{ph}}|$ equal or greater than the values reported herein for devices covering areas relevant to commercial, scalable fuel formation.⁹⁶

3.5 Conclusion

Vertically oriented Si μW arrays allowed for the integration of discontinuous, electrodeposited Cu films at mass-loadings sufficient to drive photoelectrochemical CO_2R at overpotentials comparable to a continuous planar Cu film, while maintaining stable photocurrent densities comparable to those exhibited by a planar Si surface with no Cu. Metallic catalysts that exhibit large Tafel slopes and primarily reflect, rather than absorb, light benefit from this method of semiconductor-catalyst integration. The $|J_{\text{ph}}|$ obtained at the $\text{n}^+\text{p-Si } \mu\text{W}/\text{Cu}$ electrodes under 1 Sun illumination in this work are among the highest reported values for photocathodes for CO_2R , independent of where the catalyst was located. Thus, semiconductors that can be structured into high-aspect ratio features, larger than a wavelength of light, are suitable for integration with high loadings of metallic electrocatalysts for photoelectrochemical devices.